PHYSICAL GRADIENTS FOR DEEP LEARNING

Anonymous authors
Paper under double-blind review

ABSTRACT

Solving inverse problems, such as parameter estimation and optimal control, is a vital part of science. Many experiments repeatedly collect data and employ machine learning algorithms to quickly infer solutions to the associated inverse problems. We find that state-of-the-art training techniques are not well-suited to many problems that involve physical processes since the magnitude and direction of the gradients can vary strongly. We propose a novel hybrid training approach that combines higher-order optimization methods with machine learning techniques. We replace the gradient of the physical process by a new construct, referred to as the *physical gradient*. This also allows us to introduce domain knowledge into training by incorporating priors about the solution space into the gradients. We demonstrate the capabilities of our method on a variety of canonical physical systems, showing that physical gradients yield significant improvements on a wide range of optimization and learning problems.

1 INTRODUCTION

Inverse problems that involve physical systems play a central role in computational science. This class of problems includes parameter estimation (Tarantola, 2005) and optimal control (Zhou et al., 1996). Solving inverse problems is integral in determining the age of the universe (Freedman et al., 2001), measuring the amount of dark matter (Padmanabhan & White, 2009), detecting gravitational waves (George & Huerta, 2018b), controlling plasma flows (Maingi et al., 2019), searching for neutrinoless double-beta decay (Agostini et al., 2013; Aalseth et al., 2018), reconstructing particle trajectories and energies (Belayneh et al., 2020), and testing general relativity (Dyson et al., 1920; Kraniotis & Whitehouse, 2003).

Decades of research in optimization have produced a wide range of methods and algorithms for solving inverse problems (Press et al., 2007). Higher-order methods such as limited-memory BFGS (Liu & Nocedal, 1989) have been especially successful. However, many experiments continuously or repeatedly collect data, yielding datasets with millions or billions of individual events, each posing an inverse problem. In such settings, data analysis has often turned to machine learning algorithms to quickly infer approximate solutions given the observations (Carleo et al., 2019; Delaquis et al., 2018; George & Huerta, 2018b; Agostini et al., 2013). The inferred solutions can be used to filter data sets for interesting events and can serve as the basis for more accurate analysis (CMS Collaboration, 2020; George & Huerta, 2018a;b).

Here we describe a new method for training deep learning models that is vastly more efficient than state-of-the-art training techniques for a broad class of inverse problems that involve physical processes. The improvement is based on the fact that nearly all modern deep learning methods only use first-order information (Goodfellow et al., 2016) while optimization algorithms in computational science make use of higher-order information to accelerate convergence (Ye et al., 2019). Using second-order optimizers such as Newton's method to train deep learning models typically imposes severe limitations, either significantly restricting the size of the training set or requiring the evaluation of second derivatives, which is computationally demanding (Goodfellow et al., 2016).

In this paper, we derive a hybrid optimization algorithm that integrates higher-order inverse solvers into the traditional deep learning pipeline without imposing these limitations and without discarding the progress made in first-order optimization. Our method can work with arbitrary second-order solvers when the solution space of the inverse problem allows for computation of the Hessian. Otherwise, it requires additional domain knowledge which is used to formulate the inverse solver in a

more efficient manner. The result of the embedded inverse-problem solver takes the place of the first-order gradient of the physical process, and we refer to it as the *physical gradient* (PG). When used in conjunction with training deep learning models, physical gradients allow each update step to encode nonlinear physics, which yields substantially more accurate optimization directions. A key advantage of our approach is its compatibility with acceleration schemes (Duchi et al., 2011; Kingma & Ba, 2015) and stabilization techniques (Ioffe & Szegedy, 2015; Huang et al., 2016; Ba et al., 2016) developed for training deep learning models.

The presented hybrid training approach differs fundamentally from pure first-order training. While PGs take the place of regular gradients in the optimization algorithm, they are based on real physical states instead of the adjoint ones calculated in backpropagation. This feature makes it possible to integrate solution priors into the training without restricting the model architecture (Kim et al., 2019), adding soft constraints to the objective (Raissi et al., 2018), or relying exclusively on first-order updates (Rackauckas et al., 2020).

We test our method on a wide variety of inverse problems including the highly challenging Navier-Stokes equations. In all of our experiments, neural networks trained with PGs significantly outperform state-of-the-art training schemes, yielding accuracy gains of up to three orders of magnitude.

2 METHOD

We consider unconstrained inverse problems that involve a differentiable physical process $\mathcal{P} : X \subset \mathbb{R}^{d_x} \to Y \subset \mathbb{R}^{d_y}$ which can be simulated. Here X denotes the physical parameter space and Y the space of possible observed outcomes. Given an observed or desired output $y^* \in Y$, the inverse problem consists of finding optimal parameters

$$x^* = \min_x L(x) \quad \text{with} \quad L(x) = \frac{1}{2}\|\mathcal{P}(x) - y^*\|_2^2. \tag{1}$$

We are interested in approximating this problem using a neural network, $x^* = \mathrm{NN}(y^* \,|\, \theta)$, parameterized by θ. Let $\mathcal{Y}^* = \{y_i^* \,|\, i = 1, ..., N\}$ denote a set of N inverse problems, all sharing the same physical process $\mathcal{P}$. Then training the network is equivalent to finding

$$\theta_* = \min_\theta \sum_{i=1}^{N} \frac{1}{2}\|\mathcal{P}\big(\mathrm{NN}(y_i^* \,|\, \theta)\big) - y_i^*\|_2^2 \,. \tag{2}$$

This training scheme is unsupervised, i.e. no labels are required over the training data $\mathcal{Y}$.

2.1 ITERATIVE OPTIMIZATION

Inverse problems as in Eq. 1 are classically solved by starting with an initial guess x_0 and iteratively applying updates Δx_k. This yields an estimate of the inverse of the physical model $\mathcal{P}$, i.e., $x^* = \mathcal{P}_{n^*}^{-1}(y^* \,|\, x_0)$ where n^* denotes the number of iterations required to reach a chosen convergence threshold. A key decision in such an iterative optimization scheme is how to derive the update Δx_k. Figure 1 visually compares gradient descent, Newton's method and PGs which we will discuss and compare in the following paragraphs.

First-order methods The scale of typical machine learning datasets necessitates the use of mini-batches, which has led popular optimization methods in machine learning to rely only on first-order derivatives of L. These Hessian-free methods are popular in deep learning due to their low computational cost and stable convergence (Goodfellow et al., 2016). The simplest such method is gradient descent (GD) (Curry, 1944) and its stochastic version (SGD) where $\Delta x = -\eta \cdot \left(\frac{\partial L}{\partial x}\right)^T$. Note that the dimensions of $\frac{\partial L}{\partial x}$, and therefore of Δx, are inversely proportional to the dimensions of x. Consequently, when small changes in x cause large changes in L, GD counter-intuitively produces large update steps Δx and vice versa (exploding / vanishing gradients). Machine learning models can be tuned to behave well given these updates (Ioffe & Szegedy, 2015; Loshchilov & Hutter, 2019) but in physics-based optimization, where functions may be extremely sensitive in certain parts of the parameter space or on subsets of training examples, GD often prescribes suboptimal optimization directions.

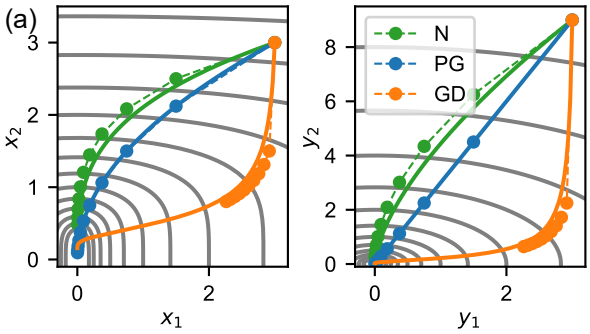

(b)	Update	S	HF	NL
GD	$-\eta \left((\mathcal{P}(x) - y^*) \frac{\partial x}{\partial \theta} \right)^T$		✓	
N	$-\eta\, H^{-1} \left((\mathcal{P}(x) - y^*) \frac{\partial x}{\partial \theta} \right)^T$	✓		✓
PG	$-\eta \left(\frac{\partial x}{\partial \theta} \right)^T \left(x - \mathcal{P}_n^{-1}(y^*) \right)^T$	✓	✓	✓

Figure 1: (a) Minimization of the function $L = \|y\|_2^2$ with $y = (x_1, x_2^2)$ in x space. Contours of L are shown in gray. Solid lines are the optimization trajectories of gradient descent (GD), Newton's method (N), and physical gradients (PG), with infinitesimal step sizes. Circles represent the first 10 iterations with constant step size. (b) Comparison of the same optimization methods by their respective update steps and properties: whether they can adapt to function sensitivity (S), are Hessian-free (HF) and take nonlinearities into account (NL). H denotes the Hessian $H = \mathcal{P}'(x) \left(\frac{\partial x}{\partial \theta}\right)^2 + (P(x) - y^*) \frac{\partial^2 x}{\partial \theta^2}$.

While there are a number of first-order optimizers that approximate higher-order information to improve convergence (Kingma & Ba, 2015; Hestenes et al., 1952; Duchi et al., 2011; Martens & Grosse, 2015), they cannot take nonlinearities into account, which results in suboptimal optimization directions when optimizing nonlinear functions.

Second-order methods Newton's method (Atkinson, 2008) uses the inverse Hessian to determine the optimization update $\Delta x = -\eta \cdot \left(\frac{\partial^2 L}{\partial x^2}\right)^{-1} \left(\frac{\partial L}{\partial x}\right)^T$. Direct computation of the Hessian adds a significant computational cost to each iteration. Quasi-Newton methods (Broyden, 1970; Liu & Nocedal, 1989; Gill & Murray, 1978; Moré, 1978; Powell, 1970; Berndt et al., 1974; Conn et al., 1991; Avriel, 2003) alleviate this issue by approximating the inverse Hessian instead. Unlike GD, Newton-type methods prescribe small updates to sensitive functions and large updates to insensitive ones. The resulting update steps typically progress towards optima much faster than first-order methods (Ye et al., 2019). However, the difficulty of approximating the Hessian for batched data sets (Schraudolph et al., 2007) and the high cost of evaluating the Hessian directly have largely prevented second-order methods from being utilized in machine learning research (Goodfellow et al., 2016).

Inverse physics via domain knowledge Domain-specific knowledge can often be used to formulate more efficient optimization updates or to directly approximate a solution. We will refer to these domain-knowledge-based $\mathcal{P}^{-1}$ as *inverse physics solvers* (for definition see appendix A.2). A classical example would be preconditioners that, when chosen correctly, allow linear solvers to converge much more quickly and reliably. In nonlinear settings, part of the governing equations may be inverted analytically or priors about the solution space may be incorporated into the solver, for example. A time-reversed simulation may be able to more accurately recover prior states than an generic inverse solver. When solving single optimization problems, these methods would replace the traditional iterative solver. However for coupled optimizations as in Eq. 2, utilizing inverse physics solvers has not yet been explored. As we will show in the following, PGs allow for a straightforward incorporation of these solvers into machine learning settings.

2.2 Physical gradients for deep learning

We now consider the problem of learning solutions to the inverse problems as in Eq. 2. As discussed above, GD-based optimizers fail to take the nonlinearity and potentially strongly varying sensitivity of the joint problem into account while higher-order optimizers are hard to apply directly.

Instead, we aim to leverage the advantages of higher-order optimizers in a deep learning setting by embedding arbitrary inverse-problem solvers as physical gradients (PGs) into the first-order op-

timization pipeline. The network updates themselves can then be computed using any first-order optimizer such as SGD or Adam. Additionally, all state-of-the-art deep learning techniques, such as normalization Ioffe & Szegedy (2015); Ba et al. (2016) or dropout Srivastava et al. (2014) can be employed, which often improves training speed and generalization performance Keskar et al. (2017).

Our method can be applied whenever one of the following is available: (i) $\frac{\partial^2 \mathcal{P}}{\partial x^2}$ can be computed numerically, (ii) a higher-order update such as $\left(\frac{\partial^2 \mathcal{P}}{\partial x^2}\right)^{-1} \frac{\partial \mathcal{P}}{\partial x}$ can be derived analytically, or (iii) an inverse-physics solver can be derived using the available domain knowledge.

We derive our method starting from Eq. 2 which describes the combined problem of finding both solutions x^* to the individual inverse problems $y^* \in \mathcal{Y}^*$ and network weights θ that approximate them. One way to solve this problem is to first consider all inverse problems separately and precompute corresponding solutions $\mathcal{X}^{\text{sup}} = \{x_i^{\text{sup}} : \mathcal{P}(x_i^{\text{sup}}) = y_i^*\}$ using an iterative optimizer. Then, $\mathcal{X}^{\text{sup}}$ could be used as labels for supervised training of a neural network:

$$\theta_* = \min_\theta \sum_{i=1}^{N} \frac{1}{2} \|\text{NN}(y_i^* \,|\, \theta) - x_i^{\text{sup}}\|_2^2. \tag{3}$$

This precomputation makes it possible to use an efficient optimization method for $\mathcal{X}^{\text{sup}}$ while training the neural network with a first-order optimizer, retaining the ability to employ state-of-the-art deep learning techniques, such as normalization (Ioffe & Szegedy, 2015; Ba et al., 2016) or dropout (Srivastava et al., 2014). However, this approach has severe drawbacks. For one, the individual optimizations can more easily get stuck in local optima than the combined training (Holl et al., 2020). Also, many inverse problems are inherently multi-modal, i.e. multiple solutions x^* exist for one y^*. In such settings x^{sup} heavily depends on the initial guess x_0 used for precomputation, which may cause the network to interpolate between possible solutions, leading to subpar convergence and generalization performance.

To avoid these problems, we alter the training procedure from Eq. 3 in two ways. First, we treat the inverse problem solver $\mathcal{P}^{-1}$ as part of a coupled optimization and consider it as part of the training loop, yielding

$$\theta_* = \min_\theta \sum_{i=1}^{N} \frac{1}{2} \|\text{NN}(y_i^* \,|\, \theta) - \mathcal{P}_{n_i^*}^{-1}(y_i^*)\|_2^2 \,. \tag{4}$$

Next we can condition the embedded inverse problem solver on the neural network prediction, $\mathcal{P}_{n_i^*}^{-1}(y_i^*) \rightarrow \mathcal{P}_{n_i^*}^{-1}(y_i^* \,|\, \text{NN}(y_i^* \,|\, \theta))$, by using it as an initial guess. The embedded optimizer can now find a minimum close to the prediction, which allows the neural network to choose any solution of a multi-modal problem. Also, since all inverse problems from $\mathcal{Y}^*$ are optimized jointly, this reduces the likelihood that an individual solution gets stuck in a local minimum.

It is furthermore not necessary to run the iterative inverse solver to convergence. Any choice of $n \in \mathbb{N}$ steps likely leads to convergence, and choosing small n can increase the training speed (proof given in appendix A.2). In all experiments, we perform only a single iteration, $n = 1$. With these modifications, we arrive at

$$\theta_* = \min_\theta \sum_{i=1}^{N} \frac{1}{2} \|\text{NN}(y_i^* \,|\, \theta) - \mathcal{P}_n^{-1}(y_i^* \,|\, \text{NN}(y_i^* \,|\, \theta))\|_2^2. \tag{5}$$

The central quantity here is the difference between prediction and correction obtained from $\mathcal{P}_n^{-1}$, which we refer to as the *physical gradient*. It encodes a valid physical state and takes the place of $\left(\frac{\partial \mathcal{P}}{\partial x}\right)^T$, which would otherwise be computed by backpropagation.

Algorithm 1 details the corresponding neural network training procedure. There, the effective gradient $\Delta\theta$ can also be written as $\frac{\partial}{\partial \theta} \frac{1}{2} \|x_0 - x_n\|_2^2$ with x_n taken as constant as in Eq. 5, which lends itself to straightforward integration into machine learning frameworks where a simple L_2 loss can be used to optimize the network. This L_2 loss acts as a proxy to embed the physical gradient into the network training pipeline and is not to be confused with a traditional supervised loss in x space (see appendix A.1 for a more detailed discussion).

Algorithm 1: Neural network training with physical gradients according to Eq. 5

for *each training sample* **do**
  $x_0 \leftarrow \mathrm{NN}(y^* \,|\, \theta)$ — Solution inference with NN
  for $k = 1, ..., n$ **do**
    $y_k \leftarrow \mathcal{P}(x_{k-1})$ — Forward simulation
    $x_k \leftarrow \mathcal{P}^{-1}(y^* \,|\, x_{k-1}, y_k)$ — Backward simulation for PG
  end
  $\Delta\theta \leftarrow \left(\frac{\partial x}{\partial \theta}\right)^T \cdot (x_0 - x_n)^T$ — Backpropagation through NN
  $\theta \leftarrow \mathrm{Step}(\theta, \Delta\theta, \eta)$ — Parameter update
end

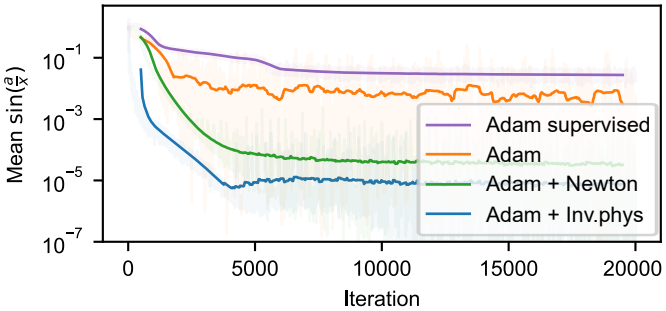

Figure 2: Network trained on single-parameter optimization using Adam in combination with various gradient schemes. Running average over 1000 mini-batches. The vertical axis is on a logarithmic scale.

3 Results

We first demonstrate the differences between various neural network training schemes on a simple one-parameter example before moving on to physical systems described by partial differential equations. We specifically consider Poisson's equation, the heat equation, and the Navier-Stokes equations. This selection covers ubiquitous physical processes with diffusion, transport, and strongly non-local effects, featuring both explicit and implicit solvers. In each experiment, we train identically-initialized networks using different gradient schemes for $\mathcal{P}$ to examine the relative differences in convergence behavior. For the weight update, we primarily employ the Adam optimizer (Kingma & Ba, 2015), a standard method in deep learning that outperforms SGD in our experiments. All training data are randomly generated on the fly, resulting in effectively infinite data sets $\mathcal{Y}$. All shown learning curves are therefore representative of the performance on unseen data. A detailed description of our experiments along with additional visualizations and performance measurements can be found in appendix B.

3.1 Single-parameter optimization

First, we consider the task of finding solutions $x^* \in \mathbb{R}$ of the inverse problem (Eq. 1) $\mathcal{P}_a(x) = \sin(\frac{a}{x})$, $y^* = -1$, given $a \in [0.1, 10.1)$. This problem may seem simple at first glance but $\mathcal{P}$ shares some properties with chaotic physical systems, which makes this problem hard to optimize. In particular: $\mathcal{P}$ is multi-modal; $\frac{\partial \mathcal{P}}{\partial x}$ is unbounded; $\mathcal{P}$ has a local minimum at $+\infty$; $\frac{\partial \mathcal{P}}{\partial x}$ and $\frac{\partial^2 \mathcal{P}}{\partial x^2}$ periodically become singular. We train a neural network with three fully-connected hidden layers to solve this task; the learning curves are shown in Fig. 2. We use $\sin(\frac{a}{x}) + 1$ as a metric for the solution quality as it reflects the multi-modality of the inverse problems and is strongly correlated with the error in both x and y space.

Supervised training schemes (Eq. 3) perform poorly on this task due to multi-modality. When the classic optimizer for precomputation starts from a random x_0, the network fails to learn because there is no single x^* to converge to. Fixing x_0 improves this behavior, but it still leads to different minima being selected depending on a, albeit in a deterministic manner. A more powerful neural

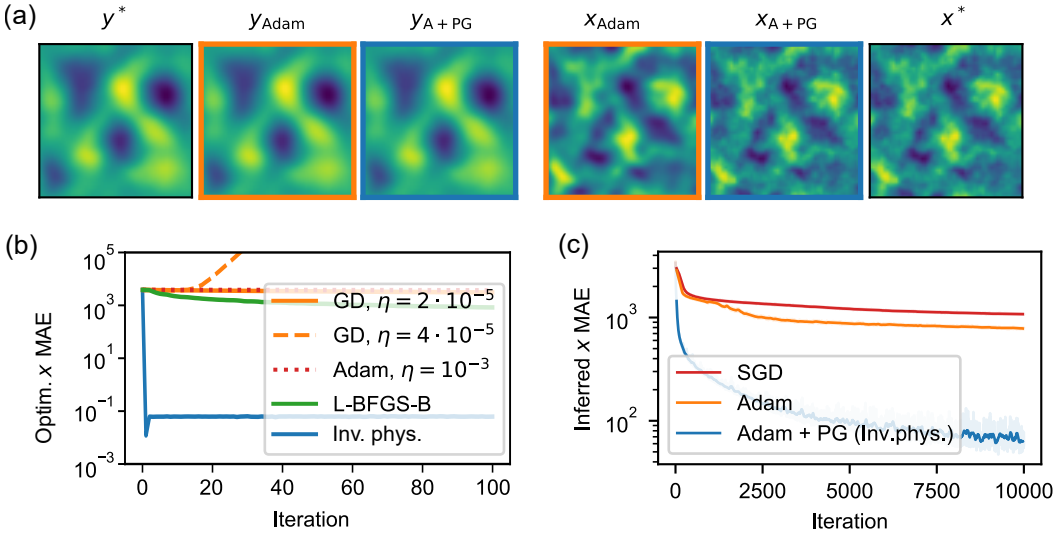

Figure 3: Optimization of Poisson's equation to reconstruct a desired output state. (a) Convergence curves of various optimization methods on a random example. (b) Neural network learning curves, running average over 64 mini-batches. The vertical axes are logarithmic.

network may be able to eventually learn these selections but we observe that learning stops after an accuracy of 10^{-1} to 10^{-2} is reached for $x_0 = 1$, and earlier for $x_0 < 1$.

Using Adam for the joint optimization – with backpropagation through the network and physics (Eq. 2) – avoids the aforementioned problem as the gradients dynamically guide the optimization towards a proximal minimum. However, $\frac{\partial \mathcal{P}}{\partial x}$ oscillates without bound when $x \to 0$, which causes overflow errors in the optimization. To avoid this, we clip the gradients $\frac{\partial \mathcal{P}}{\partial x}$ to $[-1, 1]$, which keeps the optimization relatively stable, although in most cases it never fully converges. This demonstrates one of the key weaknesses of first-order learning: when the magnitude of the gradients varies strongly between examples, the optimization is either slow or unstable, depending on the learning rate. Nevertheless, Adam outperforms the supervised learning baseline, converging to an accuracy of around 10^{-2}.

Finally, we test two variants of physical gradients (Eq. 5) on this problem. The first is Newton's method with analytically-derived updates. Since Newton's method uses the inverse Hessian, the gradients periodically diverge, which we remedy by clipping them as above. Second, we construct an inverse solver that analytically finds the solution $x^* = \mathcal{P}^{-1}(x_0)$ closest to the network prediction x_0. This requires domain knowledge.

As Fig. 2 shows, the PG methods vastly outperform both supervised and unsupervised first-order training, converging to an accuracy of around 10^{-5}. The diverging gradients in Newton's method can cause the optimization to fail despite gradient clipping, converging in less than half of the tested network initializations. In contrast, the PG variant with inverse physics converges reliably in all cases and, unlike pure GD-based optimization, it settles down to a solution without oscillating. For this example, using PG with the inverted physics results in a 1000x improvement in accuracy over conventional network training, while being more stable.

The gradients of all variants are visualized in appendix B.1.

3.2 Poisson's equation

Poisson's equation, $\mathcal{P}(x) = \nabla^{-2} x$, plays an important role in electrostatics, Newtonian gravity, and fluid dynamics (Ames, 2014). It has the property that local changes in x can affect $\mathcal{P}(x)$ globally. Here we consider a two-dimensional system and train a U-net (Ronneberger et al., 2015) to solve inverse problems (Eq. 1) on pseudo-randomly generated y^*. Fig. 3c shows the learning curves.

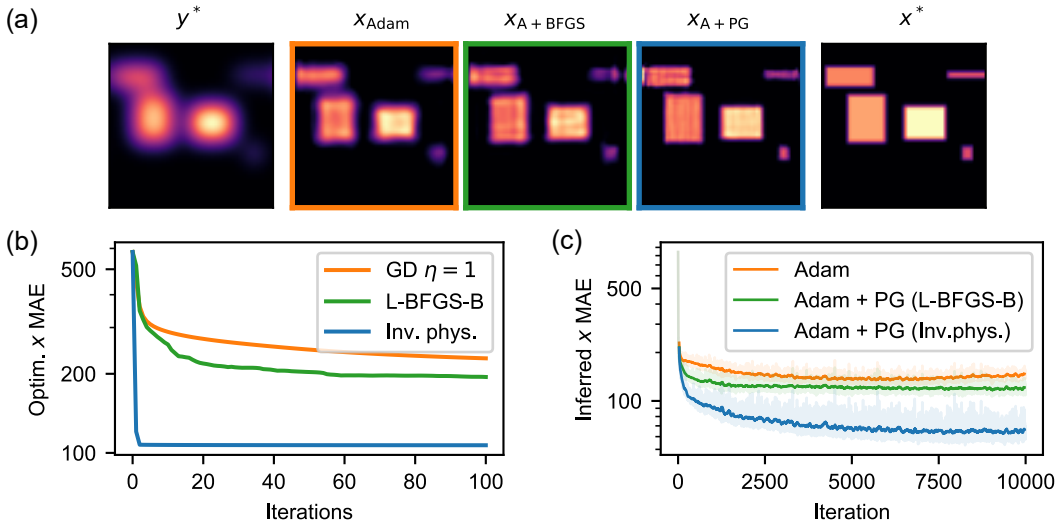

Figure 4: Optimization involving the heat equation. (a) Example from the data set: observed distribution (y^*), inferred solutions, ground truth solution (x^*). (b) Optimization curves for one example. (c) Learning curves.

First, we train the network in unsupervised fashion (Eq. 2) using both SGD with momentum and Adam. While the error initially drops quickly, learning slows after around 200 iterations for Adam and 300 iterations for SGD. Convergence remains stable, however, with Adam finding more accurate solution than SGD.

For training with PGs (Eq. 5), we consider two problem-inversion methods. In the first we use L-BFGS-B, which uses an approximation of the Hessian to perform Newton-like steps. While the dynamic choice of step size allows it to converge more quickly than GD for single problems, it is not well suited to this task because the Hessian of $\mathcal{P}$ is zero. Second, we consider the analytic inverse $\mathcal{P}^{-1} = \nabla^2$, which converges near-instantaneously for single inverse problems.

The network training with the inverse physics exhibits a vastly different behavior from the pure first-order training described above. Here, the accuracy improves much faster than with first-order methods and no sharp deceleration occurs. Instead, the learning curve closely resembles an exponential curve, which indicates linear convergence, the ideal case for first-order methods optimizing an L_2 objective. The relative performance difference compared to Adam continuously increases, from a factor of 3 at iteration 60 to a full order of magnitude after 5k iterations. During all of training, the PG variant converges exponentially faster than the first-order alternatives, in the sense that Adam or SGD take exponentially more iterations to reach a desired accuracy. Fig. 3a compares the inferred solutions of the PG and Adam networks trained for the same number of iterations to the ground truth solution. While both predictions manage to reproduce an observation similar to y^*, the PG reconstruction $x_{\text{A+PG}}$ contains noticeably more details and closely resembles the ground-truth solution. In addition, the computation of the PGs is less computationally expensive in this problem setting since $\mathcal{P}^{-1} = \nabla^2$ can be computed as a finite difference while the regular gradient requires an implicit solve.

More examples and learning curves are shown in section appendix B.2, along with a more detailed description of the experimental setup.

3.3 Heat equation

Next, we consider a system with fundamentally non-invertible dynamics. The heat equation, $\frac{\partial u}{\partial t} = \nu \cdot \nabla^2 u$, models heat flow in solids but also plays a part in many diffusive systems (Droniou, 2014). It gradually destroys information as the temperature equilibrium is approached (Grayson, 1987), causing $\nabla\mathcal{P}$ to become near-singular. Inspired by heat conduction in microprocessors, we generate examples x_{GT} by randomly scattering four to ten heat generating rectangular regions on a plane and

simulating the heat profile $y^* = \mathcal{P}(x_{\text{GT}})$ as observed from outside a heat-conducting casing. We train a U-net (Ronneberger et al., 2015) to solve the corresponding inverse problem (Eq. 1). The learning curves are shown in Fig. 4c.

Unlike with the previous example, here $\frac{\partial \mathcal{P}}{\partial x}$ is stable, and single inverse problems can be optimized with $\eta = 1$ using GD (see Fig. 4b). For the unsupervised network training (Eq. 2), we use Adam with $\eta = 10^{-3}$ and observe that the distance to the solution starts rapidly decreasing before decelerating between iterations 30 and 40 to a slow but mostly stable convergence. The sudden deceleration is rooted in the adjoint problem, which is also a diffusion problem. Backpropagation through $\mathcal{P}$ removes detail from the gradients, which makes it hard for first-order methods to recover the solution.

For training with PGs (Eq. 5), we consider L-BFGS-B and the analytically derived inverse-physics solver $\mathcal{P}^{-1}$. As with the previous example, L-BFGS-B outperforms GD when optimizing single inverse problems but reaches a limit as to the accuracy it can reach due to ill-conditioning (see Fig. 4b). While $\mathcal{P}$ can be inverted analytically, the resulting operator produces numerically highly unstable results. Instead, we use the available domain knowledge to formulate an inverse problem solver $\mathcal{P}^{-1}$ that finds approximate x^* in a stable manner by introducing probabilistic reasoning into the algorithm (see appendix B.3). This increases the computation time per training iteration by about 7% compared to evaluating the regular gradient.

Using L-BFGS-B with $n = 32$ as a PG to train the network leads to solutions that are about 20% more accurate and noticeably sharper after the same number of training iterations. This advantage is achieved early during training and stays relatively constant throughout. From iteration 40 on, L-BFGS-B training converges about as fast as pure first-order training. However, the 17x longer computation time per iteration largely negates these advantages.

The PGs based on the inverse-physics solver, on the other hand, manage to improve the convergence speed substantially. They perform on par with L-BFGS-B training for the first $\sim$35 iterations. However, afterwards the increase in accuracy does not slow down as much as with the other methods, resulting in an exponentially faster convergence. At iteration 100, the predictions are around 34% more accurate compared to Adam, and the difference increases to 130% after 10k iterations. To reach the accuracy of regular Adam training with 10k iterations, L-BFGS-B training requires 628 iterations and training with the inverse-physics solver requires only 138 iterations.

Additional examples and learning curves are shown in section appendix B.3.

3.4 Navier-Stokes equations

Fluids and turbulence are among the most challenging and least understood areas of physics due to their highly nonlinear behavior and chaotic nature (Galdi, 2011). We consider a two-dimensional system governed by the incompressible Navier-Stokes equations: $\frac{\partial v}{\partial t} = \nu \nabla^2 v - \nabla \cdot \nabla v - \nabla p$, $\nabla \cdot v = 0$, $\nabla \times p = 0$, where p denotes pressure and ν the viscosity. At $t = 0$, a region of the fluid is randomly marked with a massless colorant m_0 that passively moves with the fluid, $\frac{\partial m}{\partial t} = -v \cdot \nabla m$, and after a time t, the marker is observed again, $y^* \equiv m_t$. An example observation pair $\{m_0, y^*\}$ is shown in Fig. 5a. We target the inverse problem (Eq. 1) of finding an initial fluid velocity $x \equiv v_0$ such that $\mathcal{P}(x) = y^*$ given m_0 and m_t, where $\mathcal{P}$ simulates the time evolution of m. Since $\mathcal{P}$ is deterministic, x encodes the complete fluid flow from 0 to t. We define the objective in frequency space with lower frequencies being weighted more strongly. This definition considers the marker distribution match on all scales, from the coarse global match to fine details, and is compatible with the definition in Eq. 1. We train a U-net (Ronneberger et al., 2015) to solve these inverse problems; the learning curves are shown in Fig. 5c.

For unsupervised training (Eq. 2) with Adam, the error decreases for the first 100 iterations while the network learns to infer velocities that lead to an approximate match. The error then proceeds to decline at a much lower rate, nearly coming to a standstill. This is caused by an overshoot in terms of vorticity, as visible in Fig. 5a right. While the resulting dynamics can roughly approximate the shape of the observed m_t, they fail to match its detailed structure. Moving from this local optimum to the global optimum is very hard for the network as the distance in x space is large and the gradients become very noisy due to the highly non-linear physics. A similar behavior can also be seen when optimizing single inverse problems with GD (Fig. 5b). Here the strongly varying magnitude of the gradients poses an additional challenge for the first-order optimization, causing its progress to stall. With $\eta = 1$, it takes more than 20K iterations for GD to converge for single problems.

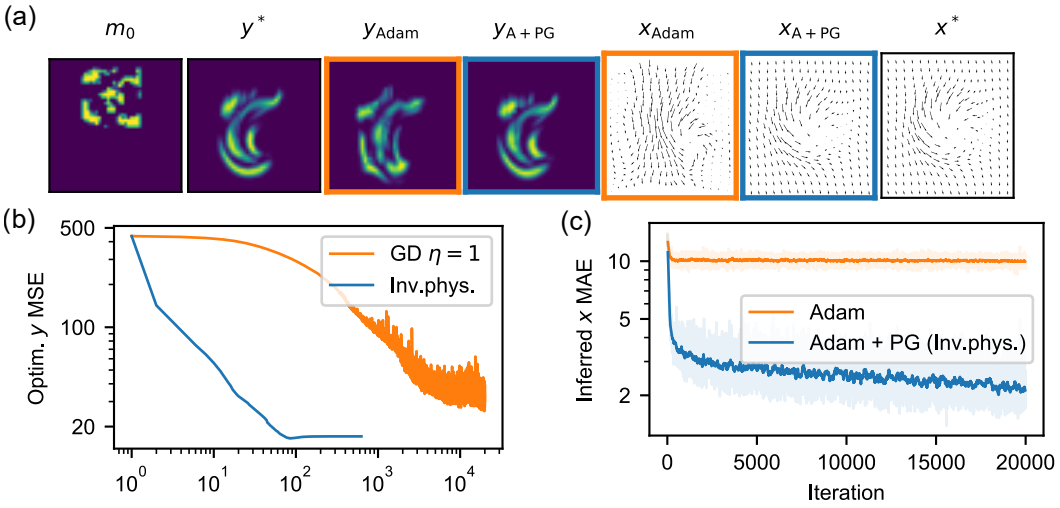

Figure 5: Incompressible fluid flow. (a) One example from the data set: initial marker distribution (m_0); simulated marker distribution after time t using ground-truth velocity (y^*) and network predictions ($y_.$); predicted initial velocities ($x_.$); ground truth velocity (x^*). (b) Optimization curves with $\eta = 1$, averaged over 4 examples. (c) Learning curves, running average over 64 mini-batches.

For training with PGs (Eq. 5), we exploit our knowledge about the flow – e.g. smoothness – to formulate an inverse simulator $\mathcal{P}^{-1}$ that incorporates corresponding priors on the solution space. It runs the simulation in reverse, starting with m_t, then estimates x by comparing the marker densities from the forward and reverse pass (see appendix B.4 for details). This method converges for single inverse problems within around 100 iterations and its computational costs are on the same level as evaluating the gradient. When used for network training, we observe vastly improved convergence behavior compared to conventional first-order training. The error rapidly decreases during the first 200 iterations, at which point the inferred solutions are more accurate than pure Adam training by a factor of 2.3. The error then continues to improve at a slower but still exponentially faster rate, reaching a relative accuracy advantage of 5x after 20K iterations. To match the network trained with pure Adam for 20K iterations, the PG variant only requires 55 iterations. This improvement is possible because the inverse-physics solver and associated PG does not suffer from the strongly-varying gradient strengths and directions, which drown the first-order signal in noise. Instead, physical gradients behave much more smoothly, both in magnitude and direction.

More examples from the fluid data set including time evolution sequences are shown in appendix B.4.

4 Conclusion

We have shown how to integrate arbitrary optimization schemes for inverse problems into machine learning settings. Our results show that first-order optimization is suboptimal in many situations, especially when the magnitude or direction of gradients can vary during the optimization or from example to example. While more advanced optimizers such as Adam alleviate this behavior, they fail to determine good optimization directions for many problems. By embedding higher-order optimizers – and especially inverse-physics solvers – into the first-order training pipeline, we were able to mitigate these shortcomings without discarding the progress made in the field of machine learning. The resulting training scheme converges exponentially faster than traditional first-order training on a wide variety of inverse problems involving partial differential equations while being on par with regular gradient evaluation in terms of computational cost.

We anticipate our method to be applicable to a wide range of differentiable processes. Beyond physics, interesting avenues lie in applying PGs to differentiable rendering or training invertible neural networks.

REPRODUCIBILITY STATEMENT

We will publish the full source code and trained network models upon acceptance. They will be sufficient to retrain the networks and plot the figures shown in this work. All data sets were generated randomly, so slight variations are expected. Repeated experiments are shown in the appendix.

REFERENCES

Craig E Aalseth, N Abgrall, Estanislao Aguayo, SI Alvis, M Amman, Isaac J Arnquist, FT Avignone III, Henning O Back, Alexander S Barabash, PS Barbeau, et al. Search for neutrinoless double-β decay in ge 76 with the majorana demonstrator. *Physical review letters*, 120(13):132502, 2018.

Martín Abadi, Paul Barham, Jianmin Chen, Zhifeng Chen, Andy Davis, Jeffrey Dean, Matthieu Devin, Sanjay Ghemawat, Geoffrey Irving, Michael Isard, et al. Tensorflow: A system for large-scale machine learning. In *12th {USENIX} symposium on operating systems design and implementation ({OSDI} 16)*, pp. 265–283, 2016.

M Agostini, M Allardt, E Andreotti, AM Bakalyarov, M Balata, I Barabanov, M Barnabé Heider, N Barros, L Baudis, C Bauer, et al. Pulse shape discrimination for gerda phase i data. *The European Physical Journal C*, 73(10):2583, 2013.

William F Ames. *Numerical methods for partial differential equations*. Academic press, 2014.

Kendall E Atkinson. *An introduction to numerical analysis*. John wiley & sons, 2008.

Mordecai Avriel. *Nonlinear programming: analysis and methods*. Courier Corporation, 2003.

Jimmy Lei Ba, Jamie Ryan Kiros, and Geoffrey E Hinton. Layer normalization. In *International Conference on Learning Representations (ICLR)*, 2016.

Dawit Belayneh, Federico Carminati, Amir Farbin, Benjamin Hooberman, Gulrukh Khattak, Miaoyuan Liu, Junze Liu, Dominick Olivito, Vitória Barin Pacela, Maurizio Pierini, et al. Calorimetry with deep learning: particle simulation and reconstruction for collider physics. *The European Physical Journal C*, 80(7):1–31, 2020.

Ernst R Berndt, Bronwyn H Hall, Robert E Hall, and Jerry A Hausman. Estimation and inference in nonlinear structural models. In *Annals of Economic and Social Measurement, Volume 3, number 4*, pp. 653–665. NBER, 1974.

Charles George Broyden. The convergence of a class of double-rank minimization algorithms 1. general considerations. *IMA Journal of Applied Mathematics*, 6(1):76–90, 1970.

Giuseppe Carleo, Ignacio Cirac, Kyle Cranmer, Laurent Daudet, Maria Schuld, Naftali Tishby, Leslie Vogt-Maranto, and Lenka Zdeborová. Machine learning and the physical sciences. *Reviews of Modern Physics*, 91(4):045002, 2019.

CMS Collaboration. A deep neural network to search for new long-lived particles decaying to jets. *Machine Learning: Science and Technology*, 1(3):035012, 2020.

Andrew R Conn, Nicholas IM Gould, and Ph L Toint. Convergence of quasi-newton matrices generated by the symmetric rank one update. *Mathematical programming*, 50(1-3):177–195, 1991.

John J Craig. *Introduction to robotics: mechanics and control*. Prentice Hall, 2005.

Haskell B Curry. The method of steepest descent for non-linear minimization problems. *Quarterly of Applied Mathematics*, 2(3):258–261, 1944.

George Cybenko. Approximation by superpositions of a sigmoidal function. *Mathematics of control, signals and systems*, 2(4):303–314, 1989.

S Delaquis, MJ Jewell, I Ostrovskiy, M Weber, T Ziegler, J Dalmasson, LJ Kaufman, T Richards, JB Albert, G Anton, et al. Deep neural networks for energy and position reconstruction in exo-200. *Journal of Instrumentation*, 13(08):P08023, 2018.

Jerome Droniou. Finite volume schemes for diffusion equations: introduction to and review of modern methods. *Mathematical Models and Methods in Applied Sciences*, 24(08):1575–1619, 2014.

John Duchi, Elad Hazan, and Yoram Singer. Adaptive subgradient methods for online learning and stochastic optimization. *Journal of machine learning research*, 12(7), 2011.

F. W. Dyson, A. S. Eddington, and C. Davidson. A Determination of the Deflection of Light by the Sun's Gravitational Field, from Observations Made at the Total Eclipse of May 29, 1919, January 1920. URL `https://doi.org/10.1098/rsta.1920.0009`.

Wendy L Freedman, Barry F Madore, Brad K Gibson, Laura Ferrarese, Daniel D Kelson, Shoko Sakai, Jeremy R Mould, Robert C Kennicutt Jr, Holland C Ford, John A Graham, et al. Final results from the hubble space telescope key project to measure the hubble constant. *The Astrophysical Journal*, 553(1):47, 2001.

Giovanni Galdi. *An introduction to the mathematical theory of the Navier-Stokes equations: Steady-state problems*. Springer Science & Business Media, 2011.

Daniel George and EA Huerta. Deep neural networks to enable real-time multimessenger astrophysics. *Physical Review D*, 97(4):044039, 2018a.

Daniel George and EA Huerta. Deep learning for real-time gravitational wave detection and parameter estimation: Results with advanced ligo data. *Physics Letters B*, 778:64–70, 2018b.

Philip E Gill and Walter Murray. Algorithms for the solution of the nonlinear least-squares problem. *SIAM Journal on Numerical Analysis*, 15(5):977–992, 1978.

Alexander Gluhovsky and Christopher Tong. The structure of energy conserving low-order models. *Physics of Fluids*, 11(2):334–343, 1999.

Ian Goodfellow, Yoshua Bengio, Aaron Courville, and Yoshua Bengio. *Deep learning*. MIT press Cambridge, 2016.

Matthew A Grayson. The heat equation shrinks embedded plane curves to round points. *Journal of Differential geometry*, 26(2):285–314, 1987.

FH Harlow. The marker-and-cell method. *Fluid Dyn. Numerical Methods*, 38, 1972.

Francis H Harlow and J Eddie Welch. Numerical calculation of time-dependent viscous incompressible flow of fluid with free surface. *The physics of fluids*, 8(12):2182–2189, 1965.

Magnus R Hestenes, Eduard Stiefel, et al. Methods of conjugate gradients for solving linear systems. *Journal of research of the National Bureau of Standards*, 49(6):409–436, 1952.

Philipp Holl, Vladlen Koltun, and Nils Thuerey. Learning to control pdes with differentiable physics. In *International Conference on Learning Representations (ICLR)*, 2020.

Gao Huang, Yu Sun, Zhuang Liu, Daniel Sedra, and Kilian Q Weinberger. Deep networks with stochastic depth. In *European conference on computer vision*, pp. 646–661. Springer, 2016.

Sergey Ioffe and Christian Szegedy. Batch normalization: Accelerating deep network training by reducing internal covariate shift. In *arXiv:1502.03167*, February 2015.

Nitish Shirish Keskar, Dheevatsa Mudigere, Jorge Nocedal, Mikhail Smelyanskiy, and Ping Tak Peter Tang. On large-batch training for deep learning: Generalization gap and sharp minima. In *International Conference on Learning Representations (ICLR)*, 2017.

Byungsoo Kim, Vinicius C Azevedo, Nils Thuerey, Theodore Kim, Markus Gross, and Barbara Solenthaler. Deep fluids: A generative network for parameterized fluid simulations. In *Computer Graphics Forum*, volume 38(2), pp. 59–70. Wiley Online Library, 2019.

Diederik Kingma and Jimmy Ba. Adam: A method for stochastic optimization. In *International Conference on Learning Representations (ICLR)*, 2015.

GV Kraniotis and SB Whitehouse. Compact calculation of the perihelion precession of mercury in general relativity, the cosmological constant and jacobi's inversion problem. *Classical and Quantum Gravity*, 20(22):4817, 2003.

Dong C Liu and Jorge Nocedal. On the limited memory bfgs method for large scale optimization. *Mathematical programming*, 45(1-3):503–528, 1989.

Ilya Loshchilov and Frank Hutter. Decoupled weight decay regularization. In *International Conference on Learning Representations (ICLR)*, 2019.

Rajesh Maingi, Arnold Lumsdaine, Jean Paul Allain, Luis Chacon, SA Gourlay, CM Greenfield, JW Hughes, D Humphreys, V Izzo, H McLean, et al. Summary of the fesac transformative enabling capabilities panel report. *Fusion Science and Technology*, 75(3):167–177, 2019.

James Martens and Roger Grosse. Optimizing neural networks with kronecker-factored approximate curvature. In *International conference on machine learning*, pp. 2408–2417. PMLR, 2015.

Jorge J Moré. The levenberg-marquardt algorithm: implementation and theory. In *Numerical analysis*, pp. 105–116. Springer, 1978.

Patrick Mullen, Keenan Crane, Dmitry Pavlov, Yiying Tong, and Mathieu Desbrun. Energy-preserving integrators for fluid animation. *ACM Transactions on Graphics (TOG)*, 28(3):1–8, 2009.

Nikhil Padmanabhan and Martin White. Calibrating the baryon oscillation ruler for matter and halos. *Physical Review D*, 80(6):063508, 2009.

Adam Paszke, Sam Gross, Soumith Chintala, Gregory Chanan, Edward Yang, Zachary DeVito, Zeming Lin, Alban Desmaison, Luca Antiga, and Adam Lerer. Automatic differentiation in pytorch. In *Advances in Neural Information Processing Systems*, pp. 1–8, 2017.

Michael Powell. A hybrid method for nonlinear equations. In *Numerical methods for nonlinear algebraic equations*. Gordon and Breach, 1970.

William H. Press, Saul A. Teukolsky, William T. Vetterling, and Brian P. Flannery. *Numerical Recipes*. Cambridge University Press, 3 edition, 2007. ISBN 9780521880688.

Christopher Rackauckas, Yingbo Ma, Julius Martensen, Collin Warner, Kirill Zubov, Rohit Supekar, Dominic Skinner, and Ali Ramadhan. Universal differential equations for scientific machine learning. In *arXiv:2001.04385*, 2020.

Maziar Raissi, Alireza Yazdani, and George Em Karniadakis. Hidden fluid mechanics: A navier-stokes informed deep learning framework for assimilating flow visualization data. *arXiv:1808.04327*, 2018.

Olaf Ronneberger, Philipp Fischer, and Thomas Brox. U-net: Convolutional networks for biomedical image segmentation. In *International Conference on Medical image computing and computer-assisted intervention*, pp. 234–241. Springer, 2015.

Nicol N Schraudolph, Jin Yu, and Simon Günter. A stochastic quasi-newton method for online convex optimization. In *Artificial intelligence and statistics*, pp. 436–443, 2007.

Andrew Selle, Ronald Fedkiw, ByungMoon Kim, Yingjie Liu, and Jarek Rossignac. An unconditionally stable maccormack method. *Journal of Scientific Computing*, 35(2-3):350–371, June 2008. ISSN 0885-7474, 1573-7691. doi: 10.1007/s10915-007-9166-4.

Nitish Srivastava, Geoffrey Hinton, Alex Krizhevsky, Ilya Sutskever, and Ruslan Salakhutdinov. Dropout: a simple way to prevent neural networks from overfitting. *The journal of machine learning research*, 15(1):1929–1958, 2014.

Albert Tarantola. *Inverse problem theory and methods for model parameter estimation*. SIAM, 2005.

Nan Ye, Farbod Roosta-Khorasani, and Tiangang Cui. Optimization methods for inverse problems. In *2017 MATRIX Annals*, pp. 121–140. Springer, 2019.

Kemin Zhou, John Comstock Doyle, Keith Glover, et al. *Robust and optimal control*, volume 40. Prentice hall New Jersey, 1996.

A METHOD

A.1 EMBEDDING THE PHYSICAL GRADIENT INTO THE GRADIENT DESCENT PIPELINE

The key for embedding inverse-physics optimizers in the machine learning pipeline is the proxy L_2 loss in Eq. 5 which passes the gradients from the physics optimizer to the GD-based neural network optimizer.

This l_2 loss may look like a supervised loss in x space but due to the dependency of the labels $\mathcal{P}^{-1}$ on the prediction, it behaves very differently. To demonstrate this, we consider the case that GD is being used as the physics optimizer. Then the total loss is purely defined in y space, reducing to a regular first-order optimization. The proxy L_2 loss simply connects the computational graphs used in backpropagation.

Physical gradients based on gradient descent are equal to unsupervised training With the shorthands $x_i = \mathrm{NN}(y_i^* \mid \theta)$, $y_i = \mathcal{P}(x_i)$ and $\Delta y_i = y_i - y_i^*$, we can write the objective functions of unsupervised training and physical gradient training as

$$U(\theta) = \sum_{i=1}^{N} \frac{1}{2} ||\Delta y_i||_2^2 \quad \text{(unsupervised)} \tag{6}$$

$$M(\theta) = \sum_{i=1}^{N} \frac{1}{2} ||x_i - \mathcal{P}^{-1}(y_i^* \mid x_i)||_2^2 \quad \text{(physical gradients)} \tag{7}$$

Theorem 1. *Minimizing $U(\theta)$ is identical to minimizing $M(\theta)$ using any gradient-descent-based optimizer if $\mathcal{P}^{-1}$ is implemented as a single gradient descent step with $\eta = 1$.*

Proof. The gradient of the unsupervised objective function is

$$\frac{\partial U}{\partial \theta} = \sum_{i=1}^{N} \Delta y_i \cdot \frac{\partial y}{\partial x} \frac{\partial x}{\partial \theta}$$

For the mixed training, we recall that the objective function of a single inverse problem is $L(x) = \frac{1}{2}||\mathcal{P}(x) - y^*||_2^2$. The corresponding gradient is $\frac{\partial L}{\partial x} = \Delta y \cdot \frac{\partial y}{\partial x}$. Inserting a gradient descent step for $\mathcal{P}^{-1}$, the gradient of the mixed objective function becomes

$$\begin{aligned}
\frac{\partial M}{\partial \theta} &= \sum_{i=1}^{N} \left(x_i - \mathcal{P}^{-1}(y_i^* \mid x_i) \right) \frac{\partial x}{\partial \theta} \\
&= \sum_{i=1}^{N} \left(x_i - \left(x_i - \eta \cdot \frac{\partial L}{\partial x} \right) \right) \frac{\partial x}{\partial \theta} \\
&= \sum_{i=1}^{N} \eta \cdot \Delta y_i \cdot \frac{\partial y}{\partial x} \frac{\partial x}{\partial \theta}
\end{aligned}$$

which is equal to $\frac{\partial U}{\partial \theta}$ for $\eta = 1$. □

This generic L_2 formulation is even applicable in settings where different parts of an end-to-end pipeline are computed by different software frameworks or hardware accelerators.

A.2 CONVERGENCE WITH PHYSICAL GRADIENTS

We consider the convergence of a coupled optimization of $L_i(x_i)$ with $x_i = f_\theta(y_i)$ involving gradient descent optimization of a general function approximator f_θ and some other optimization scheme P for minimizing objective functions $L_i(x_i)$. Here, i denotes the index of a specific example y from a data set of size N. In the context of learning to solve inverse problems, P is the inverse-problem solver on which physical gradient $P(x) - x$ is based, and f_θ represents the neural network. In the main text, we considered objectives of the form $L_i = \frac{1}{2}||\mathcal{P}(x_i) - y_i^*||_2^2$, but now we consider a more general form.

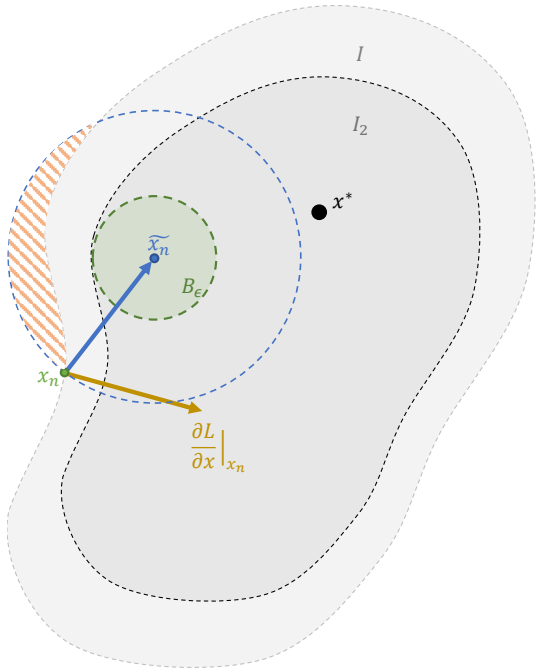

Figure 6: Convergence visualization in x space for one example i. The point $x_n = f_\theta(y)$ represents the current solution estimate. The grey line and area mark all $\{x|L(x) < L(x_n)\}$ and x^* is a minimum of L. $\tilde{x}_n = P(x_n)$ is the next point in the optimization trajectory of x and the green and blue circles around it represent open sets with radii ϵ and $||\tilde{x}_n - x_n||_2$, respectively. In the area shaded in orange, the distance to $\tilde{x}_n$ decreases but L increases.

Assumptions

1. Let $L = \{L_i : \mathbb{R}^d \to \mathbb{R} \,|\, i = 1, ..., N\}$ be a finite set of functions and let $x_i^* \in \mathbb{R}^d$ be any global minima of L_i.
2. Let $P = \{P_i : \mathbb{R}^d \to \mathbb{R}^d \,|\, i = 1, ..., N\}$ be a set of update functions for L_i such that $\exists \tau > 0 : \forall x \in \mathbb{R}^d : L_i(x) - L_i(P_i(x)) \geq \tau\,(L(x) - L(x^*))$ and $\exists K > 0 : \forall x \in \mathbb{R}^d : ||P_i(x) - x|| \leq K(L(x) - L(x^*))$.
3. Let $f_\theta : \mathbb{R}^m \to \mathbb{R}^d$ be differentiable w.r.t. θ with the property that $\exists \eta > 0 : \forall i \in 1, ..., N\ \forall x_i \in \mathbb{R}^d\ \forall \epsilon > 0\ \exists n \in \mathbb{N} : ||f_{\theta_n^{x_i}}(y_i) - x_i||_2 \leq \epsilon$ where θ_n^x is the sequence of gradient descent steps with $\theta_{n+1}^x = \theta_n^x - \eta \left(\frac{\partial f_\theta}{\partial \theta}\right)^T (f_{\theta_n} - x)$, $\eta > 0$.

Here we make minimal assumptions about L; not even continuity is required as long as we have access to some form of a physical gradient that can optimize it in x. We denote k repeated applications of P by $P^k(x)$. The assumption in (3) states that the function f_θ is flexible enough to fit our problem. It must be able to converge to every point x for all examples. This property is fulfilled even with shallow neural networks, given that sufficiently many parameters are present Cybenko (1989). We now show that P can be used in combination with gradient descent to optimize the coupled problem.

Theorem 2. *For all $k \in \mathbb{N}$, there exists an update strategy $\theta_{n+1} = U_k(\theta_n)$ based on a single evaluation of P^k for which $L(f_{\theta_n}(y_i))$ converges to a minimum x_i^* or minimum region of L_i $\forall i = 1, ..., N$.*

Proof. Dropping the example index i, we denote $\tilde{x}_n \equiv P^k(x_n)$ and $\Delta L^* = L(x_n) - L(x^*)$. Let I_2 denote the open set of all x for which $L(x) - L(x_n) > \frac{\tau}{2}\Delta L^*$ Definition (2) provides that $\tilde{x}_n \in I_2$. Since I_2 is open, $\exists \epsilon > 0 : \forall x \in B_\epsilon(\tilde{x}_n) : L(x_n) - L(x) > \frac{\tau}{2}\Delta L^*$ where $B_\epsilon(x)$ denotes the open

set containing all $x' \in \mathbb{R}^d$ for which $||x' - x||_2 < \epsilon$, i.e. there exists a small ball around $\tilde{x}_n$ which is fully contained in I_2 (see sketch in Fig. 6).

Using the convergence assumption for f_θ, definition (3), we can find a finite $n \in \mathbb{N}$ for which $f_{\theta_n} \in B_\epsilon(\tilde{x}_n)$ and therefore $L(x_n) - L(f_{\theta_n}) > \frac{\tau}{2}\Delta L^*$. We can thus use the following strategy U_k for minimizing $L(f_\theta)$: First, compute $\tilde{x}_n = P^k(x_n)$. Then perform gradient descent steps in θ with the effective objective function $\frac{1}{2}||f_\theta - \tilde{x}_n||_2^2$ until $L(x_n) - L(f_\theta) \geq \frac{\tau}{2}\Delta L^*$. With this strategy, each application of U_k reduces the loss to $\Delta L^*_{n+1} \leq (1 - \frac{\tau}{2})\Delta L^*_n$ so any arbitrary value of $L > L(x^*)$ can be reached within a finite number of steps. Definition (2) also ensures that $||P(x) - x|| \to 0$ as the optimization progresses which guarantees that the optimization converges to a minimum region. □

While this guarantees convergence, it requires potentially many gradient descent steps in θ for each physical gradient evaluation. This can be advantageous in special circumstances, e.g. when the physical gradient is more expensive to compute than an update in θ, and θ is far away from a solution. However, in many cases, we want to update the physical gradient after each update to θ. Without additional assumptions about P and f_θ, there is no guarantee in this case that L will decrease every iteration, even for infinitesimally small step sizes. Despite this, there is good reason to assume that the optimization decreases L over time.

When performing a gradient descent step in θ for the objective $\frac{1}{2}||f_\theta - \tilde{x}_n||_2^2$, the next value of f_θ must lie closer to $\tilde{x}_n$ than x_n. Assuming that, on average, the gradient descent steps do not prefer a certain direction, x_{n+1} is more likely to lie in $I = \{x \in \mathbb{R}^d \ : \ L(x) < L(x_n)\}$ than outside it. The region of increasing loss is shaded orange in Fig. 6. Since this region always fills less than half of the sphere around $\tilde{x}_n$, L is more likely to decrease than increase.

While this shows that the loss should decrease on average, it does not guarantee convergence. We now look at two specific formulations of P for which convergence to the correct solution is guaranteed. The first involves the physical gradient pointing directly towards a solution x^*. This is, for example, the case for unimodal problems when we choose k large enough. In the second case, we consider the physical gradient being aligned with the gradient descent vector in x space.

Theorem 3. *If* $\forall x \in \mathbb{R}^d \ \exists \lambda \in (0, 1] \ : \ P(x) = x + \lambda(x^* - x)$*, then the sequence* f_{θ_n} *with* $\theta_{n+1} = \theta_n - \eta \left(\frac{\partial f}{\partial \theta}\right)^T (x - P(x))$ *converges to* x^**.*

Proof. Rewriting $x - P(x) = \frac{\partial}{\partial x}\left(\frac{\lambda}{2}||x - x^*||_2^2\right)$ yields the update $\theta_{n+1} - \theta_n = -\eta \left(\frac{\partial \tilde{L}}{\partial x}\frac{\partial f}{\partial \theta}\right)^T$ where $\tilde{L} = \frac{\lambda}{2}||x - x^*||_2^2$. This describes pure gradient descent towards x^* with the gradients scaled by λ. Since $\lambda \in (0, 1]$, the convergence proof of gradient descent applies. □

Theorem 4. *If* $\forall x \in \mathbb{R}^d \ \exists \lambda \in (0, 1] \ : \ P(x) = x - \lambda \left(\frac{\partial L}{\partial x}\right)^T$*, then the sequence* f_{θ_n} *with* $\theta_{n+1} = \theta_n - \eta \left(\frac{\partial f}{\partial \theta}\right)^T (x - P(x))$ *converges to minima of* L*.*

Proof. This is equivalent to gradient descent in $L(\theta)$. Rewriting the update yields $\theta_{n+1} - \theta_n = -\eta \left(\frac{\partial f}{\partial \theta}\right)^T \left(x - \left(x - \left(\lambda \frac{\partial L}{\partial x}\right)^T\right)\right) = -\eta\lambda \left(\frac{\partial L}{\partial x}\frac{\partial f}{\partial \theta}\right)^T$ which is the gradient descent update scaled by λ. □

B EXPERIMENTS

Here, we give a more detailed description of our experiments including setup and analysis. The implementation of our experiments is based on the Φ_{Flow} (PhiFlow) framework Holl et al. (2020) and uses TensorFlow Abadi et al. (2016) and PyTorch Paszke et al. (2017) for automatic differentiation. Our code is open source and will be made available upon acceptance.

B.1 SINGLE-PARAMETER OPTIMIZATION

The optimization consists of finding $x^* = \text{argmin}_x \sin(\frac{a}{x})$. Fig. 7 shows the gradients for the case $a = 1$. The PG as well as the supervised methods require finding a solution x^* closest to an

initial guess x_0. We solve this analytically by first determining the index of the closest minimum, $n = \frac{a}{2\pi \cdot x_0} - \frac{3}{4}$ which we round to the closest integer. The furthest-out minima ($n = 0$ and $n = -1$) require special handling. Then the position of the minimum corresponding to n is $x^* = \frac{a}{3\pi/2 + 2\pi \cdot n}$.

Newton's method The analytic form of a Newton update is

$$\mathcal{P}(x) - x = -\frac{x^2 \cos(a/x)}{2x\cos(a/x) - a\sin(a/x)}$$

which approaches both minima and maxima. We alter this update to walk only towards minimum points by flipping the optimization direction so that the update points in the same direction as $\frac{\partial \mathcal{P}}{\partial x}$. Since Newton's method relies on an inversion of the Hessian, the produced physical gradients diverge where $\frac{\partial^2 \mathcal{P}}{\partial x^2} = 0$. To avoid overflow, we clip the gradients $\frac{\partial \mathcal{P}}{\partial x}$ to $[-1, 1]$ before they are backpropagated through the neural network.

Inverse gradients In addition to gradient inversion via the Hessian, we can invert the gradients directly. The principle of inverting the Jacobian is not new. Inverse kinematics applications such as controlling robots also employ first-order inversion Craig (2005). This results in a similar behavior concerning dimensions and function sensitivity as Newton-type methods. However, this first-order inversion cannot directly be applied to general optimization tasks because the Jacobian of a scalar objective function is a row vector. For this specific inverse problem, however, the gradient can be inverted because only a single parameter is optimized. The physical gradient is computed as

$$\mathcal{P}(x) - x = -\frac{h}{\nabla \mathcal{P}} = -x^2 \, \frac{\sin(a/x) + 1}{a\cos(a/x)}$$

where $h = \sin\left(\frac{a}{x}\right) + 1$ measures the height above y^*. It approaches $\pm\infty$ when $\sin(\frac{a}{x})$ is maximal. This inversion requires domain knowledge since h is based on the fact that $\min \mathcal{P} = -1$. Like with Newton's method, we apply gradient clipping to bound diverging inverse gradients.

Neural network training We set up a multilayer perceptron with a single input and output as well as three hidden layers containing 10, 20 and 10 neurons, respectively. This adds up to 461 total trainable parameters. A bias is applied at each layer and the ReLU activation function is applied after each hidden layer. The network is trained using Adam with a learning rate of 0.002 and mini-batches containing 1000 uniformly sampled $a \in [0.1, 10.1]$. We use Φ_{Flow} together with PyTorch to train the neural network in this experiment.

Learning curves for different network initializations are shown in Fig. 8 and the recorded computation times are shown in Fig. 12. While supervised training shows very consistent behavior across training runs, the convergence curves of Adam show more erratic behavior. Training with PGs based on the analytic solver converges in all cases, but does not always reach the same level of accuracy. While yielding superior accuracy than pure Adam for the large majority of tested initializations, it sometimes stops converging to an accuracy larger than 10^{-4}. This is most likely caused by numerical effects of the inverse solver. Training with physical gradients based on Newton's method or inverse gradients yields a convergence that strongly depends on the network initialization. This variant converges only for certain initializations. However, upon convergence, it typically reaches an accuracy similar to the inverse physics variant.

B.2 Poisson's equation

We consider Poisson's equation, $\nabla^2 y = x$ where x is the initial state and y is the output of the simulator. We set up a two-dimensional simulation with 80 by 60 cubic cells. Our simulator computes $y = \mathcal{P}(x) = \nabla^{-2} x$ implicitly via the conjugate gradient method. The inverse problem consists of finding an initial value x^* for a given target y^* such that $\nabla^2 y^* = x^*$. We formulate this problem as minimizing $L(x) = ||\mathcal{P}(x) - y^*||_2^2 = ||\nabla^{-2}(x - x^*)||_2^2$. We now investigate the computed updates Δx of various optimization methods for this problem.

Gradient descent Gradient descent prescribes the update $\Delta x = -\eta \cdot \left(\frac{\partial L}{\partial x}\right)^T = -\eta \cdot \nabla^{-2}\left(y - y^*\right)$ which requires an additional implicit solve for each optimization step. This backward solve produces

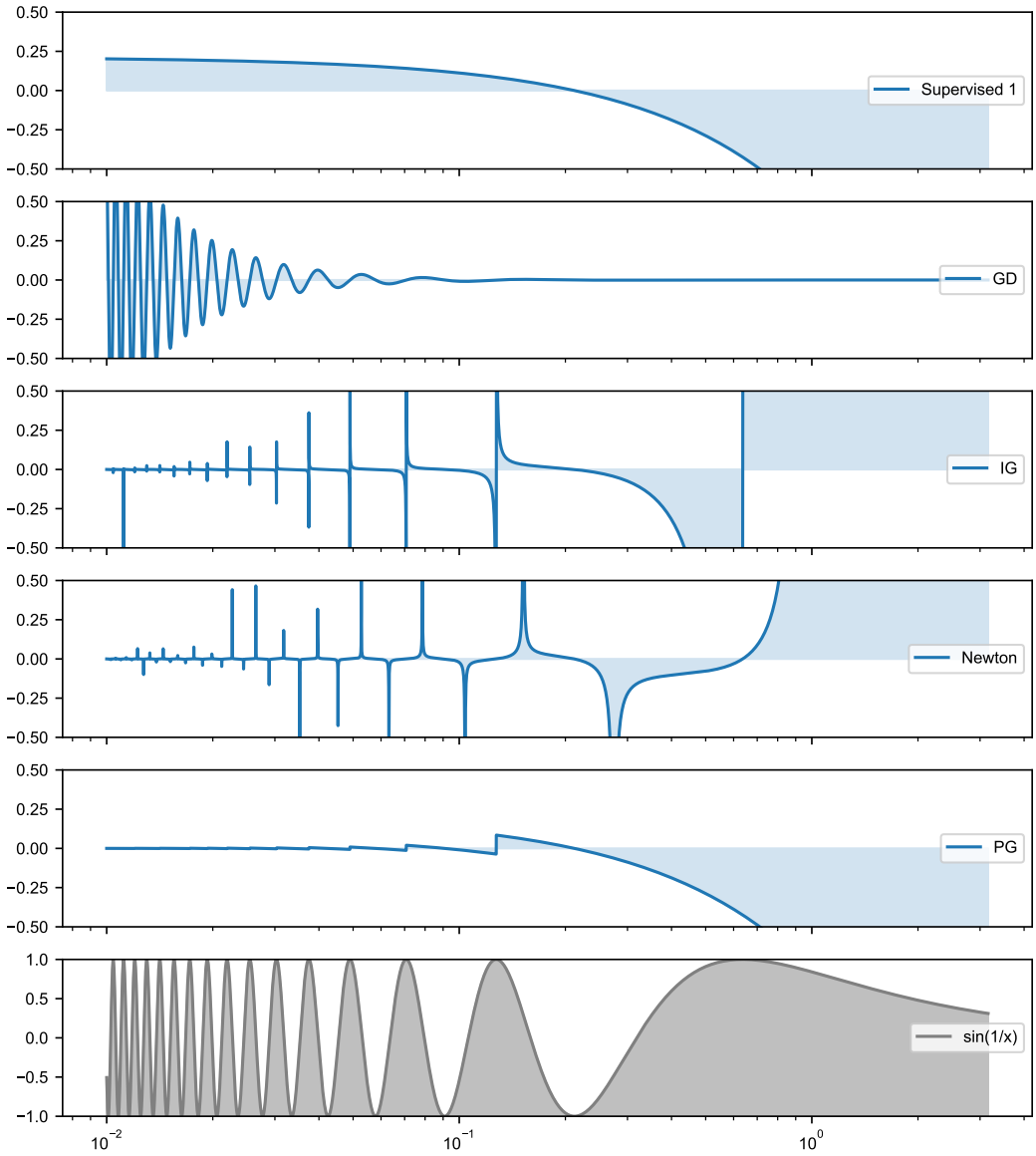

Figure 7: Gradients for minimizing $\sin(a/x)$, shown for $a = 1$. From top to bottom: Supervised learning with $x_0 = 1$, Gradient descent, inverse gradient, Newton's method, physical gradient, objective function. Singularities for small x are not properly resolved in the IG / Newton plots.

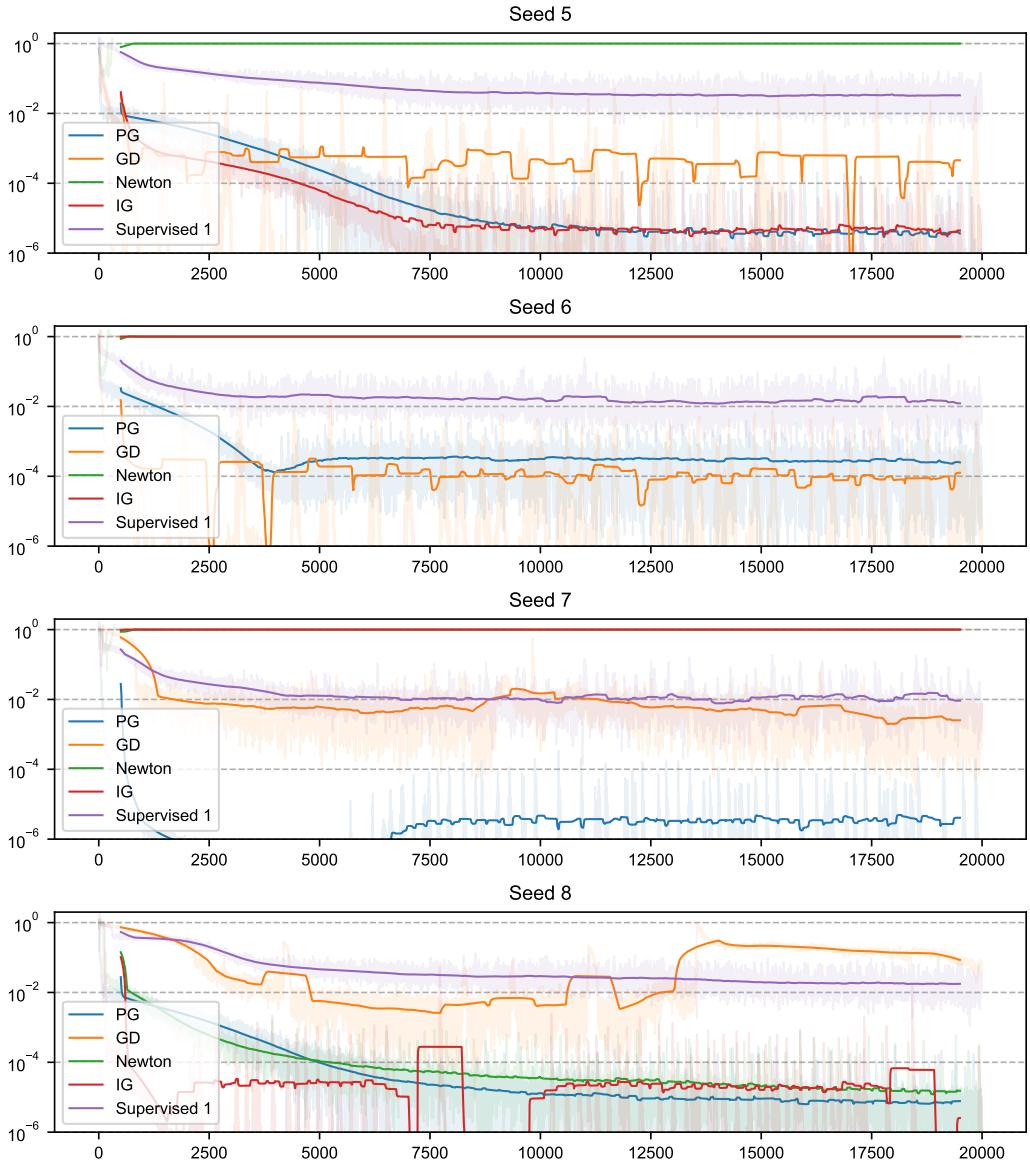

Figure 8: Networks trained on single-parameter optimization using Adam and various gradient schemes. Each figure shows the learning curves for a network initialized with a fixed seed between 5 and 8. The x axis denotes the number of training iterations, Solid lines show the running average over 1000 mini-batches.

much larger values than the forward solve, causing GD-based methods to diverge from oscillations unless η is very small. We found that GD requires $\eta \leq 2 \cdot 10^{-5}$, while the momentum in Adam allows for larger η. For both GD and Adam, the optimization converges extremely slowly, making GD-based methods unfeasible for this problem.

Physical gradients via analytic inversion Poisson's equation can easily be inverted analytically, yielding $x = \nabla^2 y$. Correspondingly, we formulate the update step as $\Delta x = -\eta \cdot \frac{\partial x}{\partial y} \cdot (y - y^*) = -\eta \cdot \nabla^2 (y - y^*)$ which directly points to x^* for $\eta = 1$. Here the Laplace operator appears in the computation of the optimization direction. This is much easier to compute numerically than the Poisson operator used by gradient descent. Consequently, no additional implicit solve is required for the optimization and the cost per iteration is less than with gradient descent. This computational advantages also carries over to neural network training where this method can be integrated into the backpropagation pipeline as a physical gradient.

Neural network training We first generate ground truth solutions x^* by adding fluctuations of varying frequencies with random amplitudes. From these x^*, we compute $y^* = \mathcal{P}(x^*)$ to form the set of target states $\mathcal{Y}$. Both generation of x^* and y^* is performed on the fly, resulting in a data set of effectively infinite size, $|\mathcal{Y}| = \infty$. This has the advantage that learning curves are representative of both test performance as well as training performance. The top of Fig. 9 shows some examples generated this way. We train a U-net Ronneberger et al. (2015) with a total of 4 resolution levels and skip connections. The network receives the feature map y^* as input. Max pooling is used for downsampling and bilinear interpolation for upsampling. After each downsampling or upsampling operation, two blocks consisting of 2D convolution with kernel size of 3x3, batch normalization and ReLU activation are performed. All of these convolutions output 16 feature maps and a final 1x1 convolution brings the output down to one feature map. The network contains a total of 37,697 trainable parameters.

For SGD and Adam training, the composite gradient of $\text{NN} \circ \mathcal{P}$ is computed with TensorFlow or PyTorch, enabling an end-to-end optimization. The learning rate is set to $\eta = 10^{-3}$ with Adam and $\eta = 10^{-9}$ for SGD. The extremely small learning rate for SGD is required to balance out the large gradients and is consistent with the behavior of gradient-descent optimization on single examples where an $\eta = 2 \cdot 10^{-5}$ was required. We use a typical value of 0.9 for the momentum of SGD and Adam. For the training using Adam with physical gradients, we compute Δx as described above and keep $\eta = 10^{-3}$. For each case, we set the learning rate to the maximum value that consistently converges. The learning curves for three additional random network initializations are shown at the bottom of Fig. 9, while Fig. 12 shows the computation time per iteration.

B.3 Heat equation

We consider a two-dimensional system governed by the heat equation $\frac{\partial u}{\partial t} = \nu \cdot \nabla^2 u$. Given an initial state $x = u_0$ at t_0, the simulator computes the state at a later time t_* via $y = u_* = \mathcal{P}(x)$. Exactly inverting this system is only possible for $t \cdot \nu = 0$ and becomes increasingly unstable for larger $t \cdot \nu$ because initially distinct heat levels even out over time, drowning the original information in noise. Hence the Jacobian of the physics $\frac{\partial y}{\partial x}$ is near-singular. In our experiment we set $t \cdot \nu = 8$ on a domain consisting of 64x64 cells of unit length. This level of diffusion is challenging, and diffuses most details while leaving the large-scale structure intact.

We apply periodic boundary conditions and compute the result in frequency space where the physics can be computed analytically as $\hat{y} = \hat{x} \cdot e^{-k^2(t_* - t_0)}$ where $\hat{y}_k \equiv \mathcal{F}(y)_k$ denotes the k-th element of the Fourier-transformed vector y. Here, high frequencies are dampened exponentially. The inverse problem can thus be written as minimizing $L(x) = ||\mathcal{P}(x) - y^*||_2^2 = ||\mathcal{F}^{-1}\left(\mathcal{F}(x) \cdot e^{-k^2(t_* - t_0)}\right) - y^*||_2^2$

Gradient descent Using the analytic formulation, we can compute the gradient descent update as

$$\Delta x = -\eta \cdot \mathcal{F}^{-1}\left(e^{-k^2(t_* - t_0)} \mathcal{F}(y - y^*)\right).$$

GD applies the forward physics to the gradient vector itself, which results in updates that are stable but lack high frequency spatial information. Consequently, GD-based optimization methods con-

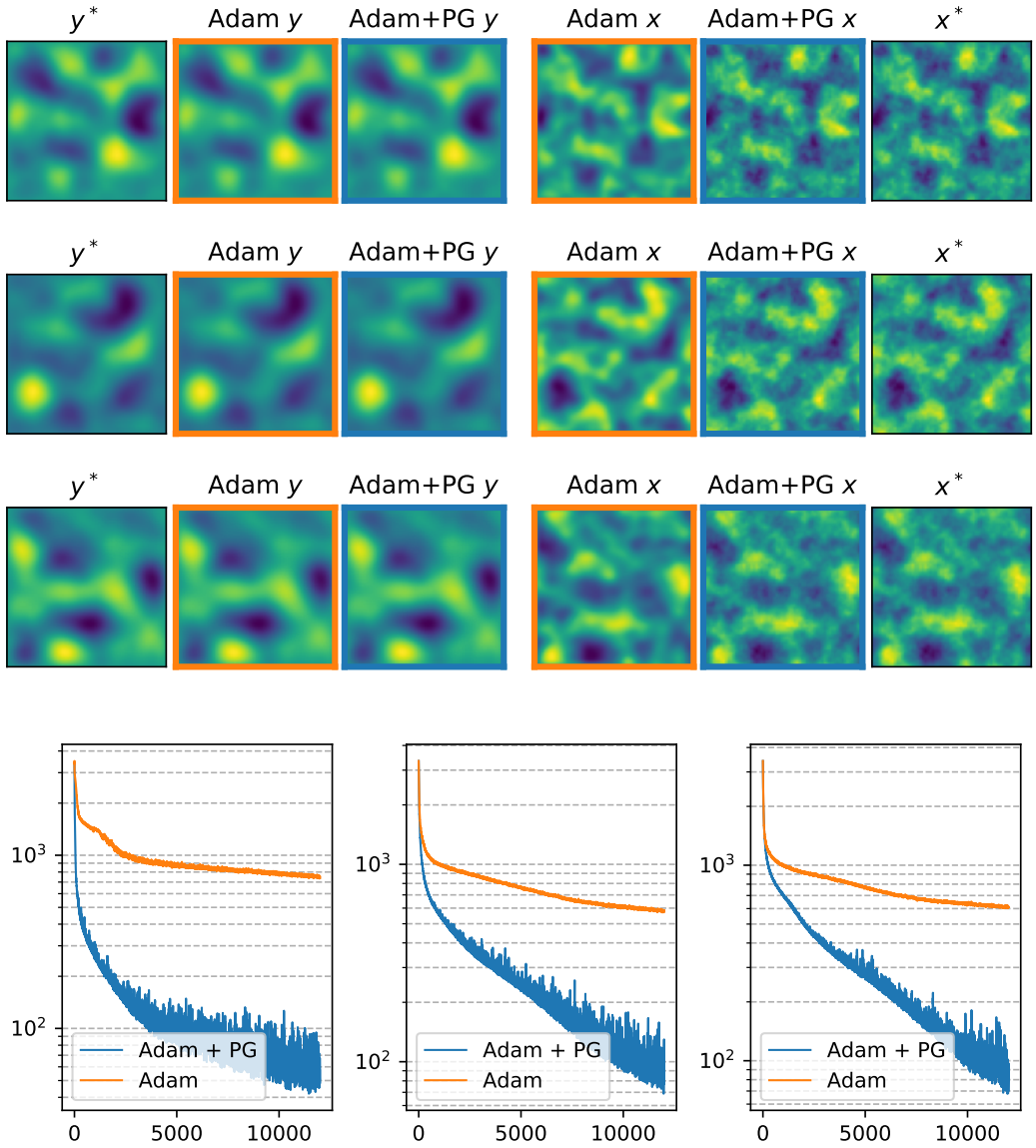

Figure 9: Inverse problems involving Poisson's equation. **Top:** Three examples from the data set, from left to right: observed target (y^*), simulated observations resulting from network predictions (Adam y, Adam+PG y), predicted solutions (Adam x, Adam+PG x), ground truth solution (x^*). Networks were trained for 12k iterations. **Bottom:** Neural network learning curves for three random network initializations, measured as $||x - x^*||_1$.

verge slowly on this task after fitting the coarse structure and have severe problems in recovering high-frequency details. This is not because the information is fundamentally missing but because GD cannot adequately process high-frequency details.

Stable physical gradients The frequency formulation of the heat equation can be inverted analytically, yielding $\hat{x}_k = \hat{y}_k \cdot e^{k^2(t_*-t_0)}$. This allows us to define the update

$$\Delta x = -\eta \cdot \mathcal{F}^{-1}\left(e^{k^2(t_*-t_0)}\mathcal{F}(y-y^*)\right).$$

Here, high frequencies are multiplied by exponentially large factors, resulting in numerical instabilities. When applying this formula directly to the gradients, it can lead to large oscillations in Δx. This is the opposite behavior compared to Poisson's equation where the GD updates were unstable and the PG stable.

The numerical instabilities here can, however, be avoided by taking a probabilistic viewpoint. The observed values y contain a certain amount of noise n, with the remainder constituting the signal $s = y - n$. For the noise, we assume a normal distribution $n \sim \mathcal{N}(0, \epsilon \cdot y)$ with $\epsilon > 0$ and for the signal, we assume that it arises from reasonable values of x so that $y \sim \mathcal{N}(0, \delta \cdot e^{-k^2})$ with $\delta > 0$. With this, we can estimate the probability of an observed value arising from the signal using Bayes' theorem $p(s|v) = \frac{p(v|s)\cdot p(s)}{p(v|s)\cdot p(s)+p(v|n)\cdot p(n)}$ where we assume the priors $p(s) = p(n) = \frac{1}{2}$. Based on this probability, we dampen the amplification of the inverse physics which yields a stable inverse. Gradients computed in this way hold as much high-frequency information as can be extracted given the noise that is present. This leads to a much faster convergence and more precise solution than any generic optimization method.

Neural network training For training, we generate x^* by randomly placing between 4 and 10 hot rectangles of random size and shape in the domain and computing $y = \mathcal{P}(x^*)$. Both operations are executed on the fly so that $|\mathcal{Y}| = \infty$ and the learning curves are representative of both training and test performance. For the neural network, we use the same U-net architecture as in the previous experiment. We train with a batch size of 128 and a constant learning rate of $\eta = 10^{-3}$. The network updates are computed with TensorFlow's or PyTorch's automatic differentiation. Fig. 10 shows two examples from the data set, along with the corresponding inferred solutions, as well as the network learning curves for two network initializations. The measured computation time per iteration is shown in Fig. 12.

B.4 Navier-Stokes equations

Here, we give additional details on the simulation, data generation, physical gradients and network training procedure for the fluid experiment.

Simulation details We simulate the fluid dynamics using a direct numerical solver. We adopt the marker-in-cell (MAC) method Harlow & Welch (1965); Harlow (1972) which guarantees stable simulations even for large velocities or time increments. The velocity vectors are sampled in staggered form at the face centers of grid cells while the marker density is sampled at the cell centers. The initial velocity v_0 is specified at cell centers and resampled to a staggered grid for the simulation. Our simulation employs a second-order advection scheme Selle et al. (2008) to transport both the marker and the velocity vectors. This step introduces significant amount of numerical diffusion which can clearly be seen in the final marker distributions. Hence, we do not numerically solve for adding additional viscosity. Incompressibility is achieved via Helmholz decomposition of the velocity field using a conjugate gradient solve.

Neither pressure projection nor advection are energy-conserving operations. While specialized energy-conserving simulation schemes for fluids exist Gluhovsky & Tong (1999); Mullen et al. (2009), we instead enforce energy conservation by normalizing the velocity field at each time step to the total energy of the previous time step. Here, the energy is computed as $E = \int_{\mathbb{R}^2} dx v(x)^2$ since we assume constant fluid density.

Data generation The data set consists of marker pairs $\{m_0, m_t\}$ which are randomly generated on-the-fly. For each example, a center position for m_0 is chosen on a grid of 64x64 cells. m_0 is then

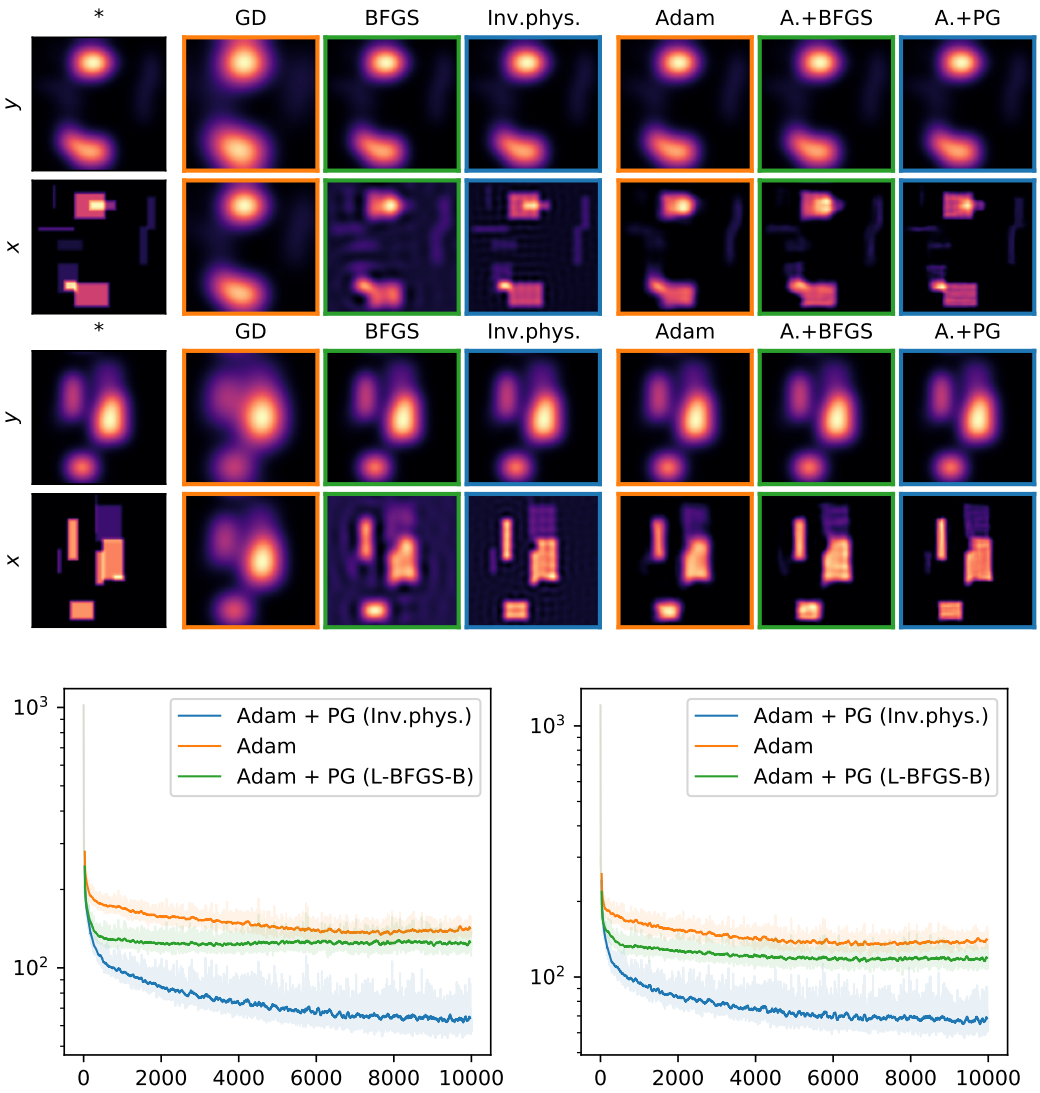

Figure 10: Inverse problems involving the heat equation. **Top:** Two examples from the data set. The top row shows observed target (y^*) and simulated observations resulting from inferred solutions. The bottom row shows the ground truth solution (x^*) and inferred solutions. From left to right: ground truth; gradient descent (GD), L-BFGS-B (BFGS) and inverse physics (Inv.phys.), running for 100 iterations each, starting with $x_0 = 0$; Networks trained for 10k iterations. **Bottom:** Neural network learning curves for two random network initializations, measured in terms of $||x - x^*||_1$.

generated from discretized noise fluctuations to fill half the domain size in each dimension. The number of marked cells is random.

Next, a ground truth initial velocity v_0 is generated from three components. First, a uniform velocity field moves the marker towards the center of the domain to avoid boundary collisions. Second, a large vortex with random strength and direction is added. The velocity magnitude of the vortex falls off with a Gaussian function depending on the distance from the vortex center. Third, smaller-scale vortices of random strengths and sizes are added additionally perturb the flow fields. These are generated by assigning a random amplitude and phase to each frequency making up the velocity field. The range from which the amplitudes are sampled depends on the magnitude frequency.

Given m_0 and v_0, a ground truth simulation is run for $t = 2$ with $\Delta t = 0.25$. The resulting marker density is then used as the target for the optimization. This ensures that there exists a solution for each example.

Computation of physical gradients To compute the physical gradients for this example, we construct an explicit formulation for $\mathcal{P}^{-1}(m_0, m_t \,|\, x_0)$ that produces an estimate for v_0 by locally inverting the physics. From this information, it fits the coarse velocity, i.e. the uniform velocity and the vortex present in the data. This use of domain knowledge, i.e., enforcing the translation and rotation components of the velocity field as a prior, is what allows it to produce a much better estimate of v_0 than the regular gradient. More formally, it assumes that the solution lies on a manifold that is much more low-dimensional than v_0. On the other hand, this estimator ignores the small-scale velocity fluctuations which limits the accuracy it can achieve. However, the difficulty of fitting the full velocity field without any assumptions outweighs this limitation. Nevertheless, GD could eventually lead to better results if trained for an extremely long time.

To estimate the vortex strength, the estimator runs a reverse Navier-Stokes simulation. The reverse simulation is initialized with the marker $m_t^{\text{rev}} = y^*$ and velocity $v_t^{\text{rev}} = v^t$ from the forward simulation. The reverse simulation then computes m^{rev} and v^{rev} for all time steps by performing simulation steps with $\Delta t = -0.25$. Then, the update to the vortex strength is computed from the differences $m^{\text{rev}} - m$ at each time step and an estimate of the vortex location at these time steps.

Neural network training We train a U-net Ronneberger et al. (2015) similar to the previous experiments but with 5 resolution levels. The network contains a total of 49,570 trainable parameters. The network is given the observed markers m_0 and m_t, resulting in an input consisting of two feature maps. It outputs two feature maps which are interpreted as a velocity field sampled at cell centers.

The objective function is defined as $|\mathcal{F}(\mathcal{P}(x) - y^*)| \cdot w$ where $\mathcal{F}$ denotes the two-dimensional Fourier transform and w is a weighting vector that factors high frequencies exponentially less than low frequencies.

We train the network using Adam with a learning rate of 0.005 and mini-batches containing 64 examples each, using PyTorch's automatic differentiation to compute the weight updates. we found that second-order optimizers like L-BFGS-B yield no significant advantage over gradient descent, and typically overshoot in terms of high-frequency motions. Example trajectories and reconstructions are shown in Fig. 11 and performance measurements are shown in Fig. 12.

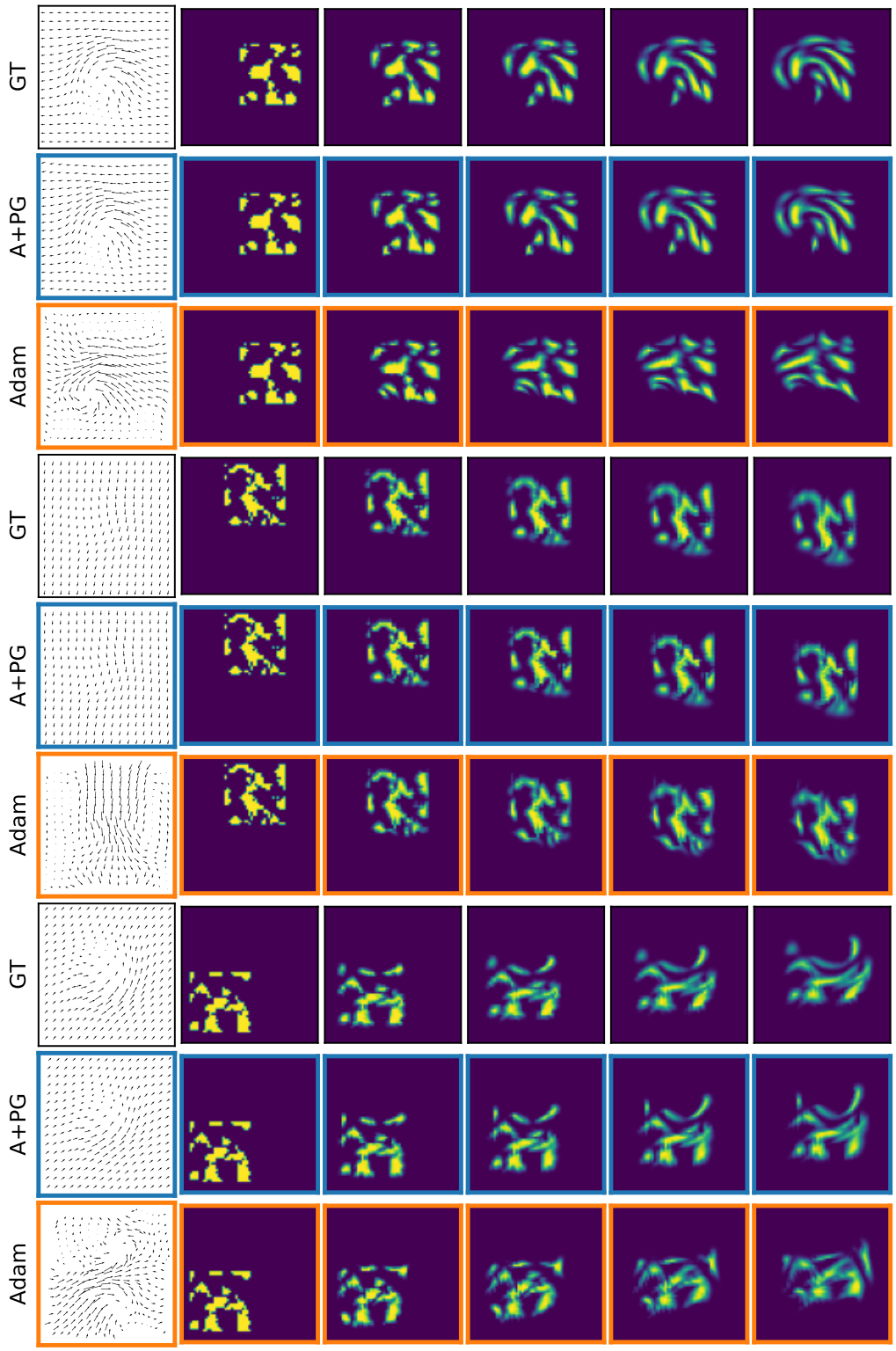

Figure 11: Three example inverse problems involving the Navier-Stokes equations. For each example, the ground truth (GT) and neural network reconstructions using Adam with physical gradient (A+PG) and pure Adam training (Adam) are displayed as rows. Each row shows the initial velocity $v_0 \equiv x$ as well as five frames from the resulting marker density sequence $m(t)$, at time steps $t \in \{0, 0.5, 1, 1.5, 2\}$. The differences of the Adam version are especially clear in terms of v_0.

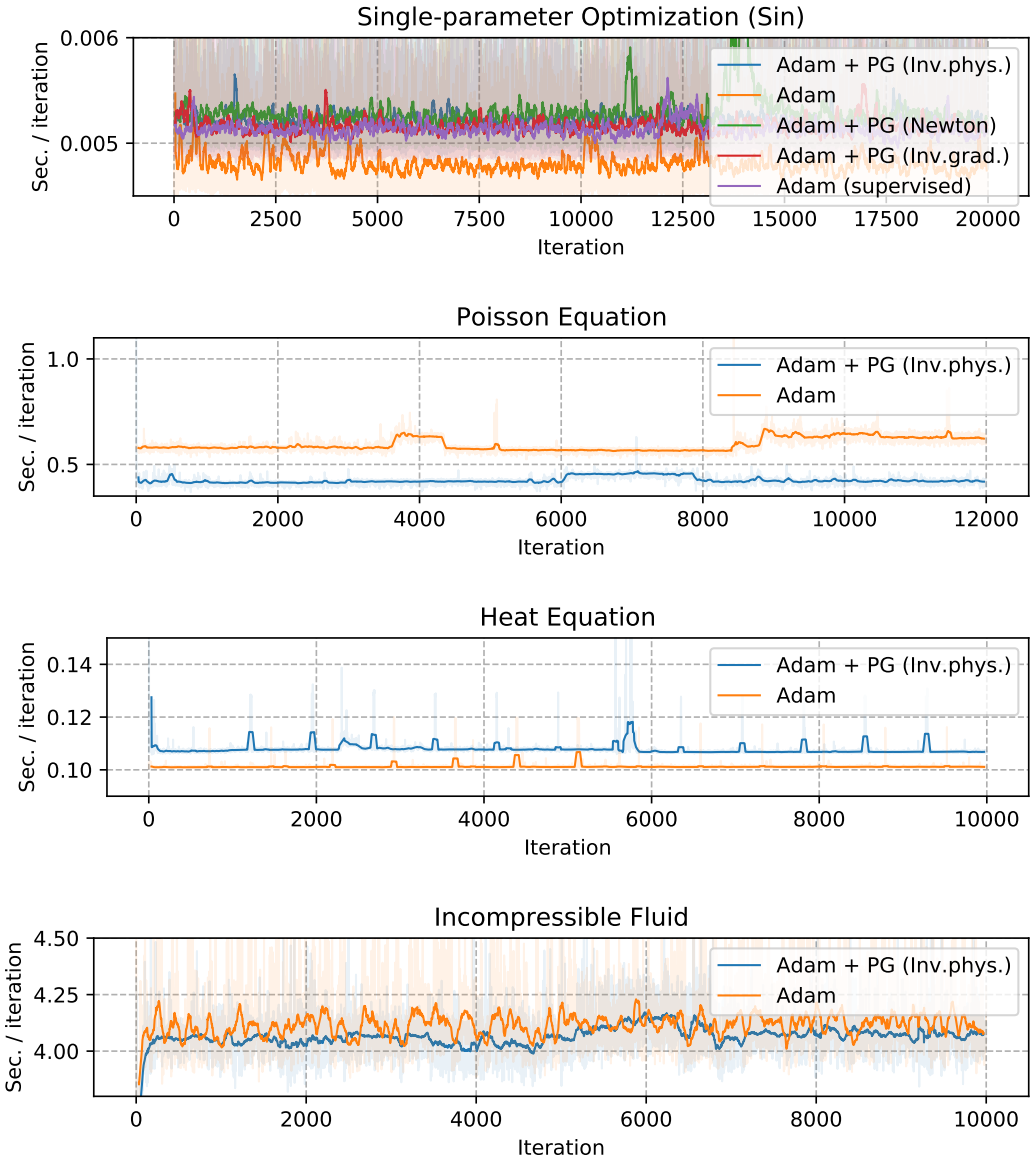

Figure 12: Measured time per neural network training iteration for all experiments, averaged over 64 mini-batches. Step times were measured using Python's `perf_counter()` function and include data generation, gradient evaluation and network update. In all experiments, the computational cost difference between the various gradients is marginal, affecting the overall training time by less than 10%.